

Two-dimensional electron gas in a metal/amorphous oxide interface with spin orbit interaction

Jose Manuel Flores-Camacho,^{1,*} Jorge Puebla,^{2,†} Florent Auvray,^{2,3} Alfonso Lastras-Martínez,¹ Yoshichika Otani,^{2,3} and Raul Eduardo Balderas-Navarro¹

¹*Instituto de Investigación en Comunicación Óptica,*

Universidad Autónoma de San Luis Potosí, Álvaro Obregón 64, 78000 San Luis Potosi, Mexico

²*Center for Emergent Matter Science, RIKEN, Wako, Saitama 351-0198, Japan*

³*Institute for Solid State Physics, University of Tokio, Kashiwa, Chiba 277-8581, Japan*

(Dated: January 13, 2020)

The formation of novel two-dimensional electron gas (2DEG) with high mobility in metal/amorphous interfaces has motivated an ongoing debate regarding the formation and novel characteristics of these 2DEGs. Here we report an optical study, based on infrared spectroscopic ellipsometry, of nonmagnetic metal and amorphous semiconducting oxide (Cu/Bi₂O₃) interfaces that confirms the formation of a 2DEG with spin orbit coupling (SOC). The 2DEG optical response was simulated with a uniaxial diagonal dielectric tensor within a sub-nanometer thin layer, where its x and z components lineshapes resolved in both free-electron and peak-like contributions, resulted very similar to theoretical predictions [M. Xie *et al.*, Phys. Rev. B **89**, 245417 (2014)] of a two dimensional electron gas confined in the normal direction of a perovskite interface. In particular, the small but finite conducting character of the z component provides a unambiguous signature of the presence of the 2DEG in the Cu/Bi₂O₃ system. Although the original constituent materials do not possess spin-orbit coupling (SOC), the resulting interfacial hybridization of such states induce electronic asymmetric wave functions. This work demonstrates the detection of 2DEG in amorphous crystals allowing to study its challenging interfacial phenomena such as SOC and interface-bulk coupling, overcoming an experimental impediment which has hold back for decades important advancements for the understanding of 2DEGs in amorphous materials.

PACS numbers: 78.68.+m, 73.20.-r, 73.40.-c, 71.70.Ej

I. INTRODUCTION

The concept of two-dimensional electron gas (2DEG) has contributed enormously to the understanding of the rich phenomena of electrons confined at surfaces and interfaces. In high quality semiconductor heterostructures, 2DEG confinement induced enhancement of electron mobility leading to technology advancements and scientific discoveries, such as the fractional Quantum Hall effect.¹ The continuous development of growth techniques allows nowadays to obtain enough good quality heterostructures from oxides, forming novel 2DEGs. Interestingly, 2DEG in oxides show a significant increase in electron density and strong electron correlation, with consequences in magnetic properties, superconductivity, ferroelectricity and spin orbit interaction.^{2,3} Intrinsically, the electronic structure of 2DEG in oxide interfaces is different from the most standard semiconductor counterparts. In most of the oxide interfaces, the transport properties are dominated by narrow d -band electrons, whereas in semiconductors the electrons localized at states at the bottom of the conduction band dictate the properties of the 2DEGs. However, despite of the great advance in the understanding of 2DEG in complex oxide interfaces, still many oxide interfaces are challenging to characterize, mainly because their crystal quality. Analysis of the electronic structure is commonly achieved by angle-resolved photoemission spectroscopy (ARPES). However, ARPES characterization requires high quality, large and flat crystals. For

instance, high quality crystals of bismuthates were obtained, allowing detailed characterization by ARPES and revealing the mechanism of its high temperature superconductivity, an open discussion for more than 30 years.⁴

Moreover, the formation of novel 2DEG with high mobility in amorphous oxides has motivated an increasing interest.^{5,6} The origin of the 2DEG formation at these interfaces has been assigned to electronic reconstruction via interfacial charge transfer;⁷ however, detailed characterization of the properties of 2DEGs formed by amorphous oxides is still lacking. An alternative to ARPES characterization is to analyze the optical conductivity of the 2DEGs by polarized spectroscopy techniques such as spectroscopic ellipsometry. Although, structural distortion and defects in amorphous materials may cause complex dielectric screening, and significantly complicate the analysis of the properties of the 2DEG, a theoretical model can be assessed and improved by direct feedback from optical characterization.⁸

Here, we report on mid-infrared ellipsometry characterization of the properties of 2DEG formed at the interface between a nonmagnetic metal and amorphous semiconducting oxide, Cu/Bi₂O₃. Recent spin-charge interconversion experiments suggest the presence of a 2DEG with spin orbit coupling (SOC) at this interface,⁹⁻¹¹ making it a very attractive structure for spin based complementary metal-oxide semiconductor technologies (CMOS).^{12,13} The characterization by angle resolved ellipsometry confirms the formation of a 2DEG

with SOC. In-depth analysis of the optical conductivity, modeled by a realistic electronic structure system and Kubo formalism, allows to define the origin of SOC as the hybridization of interfacial Cu-O-Bi states by charge transfer, generating an asymmetric wave function,¹¹ as previously suggested for amorphous perovskite oxides.^{6,7}

The rest of the paper is organized as follows. The main and reference samples are described in Sec. II together with a brief description of the ellipsometry technique. In Sec. III we present the dielectric functions of the stacked system and the model for the tensorial dielectric function of the 2DEG forming at the Cu/Bi₂O₃ interface. Finally, results and discussion are given in Sec. IV.

II. EXPERIMENT

The samples consist of Bi₂O₃ films, with thickness of 20 nm, grown on a previously (either 10, 20, or 50 nm thick) Cu-capped SiO₂/Si(001) substrate as described elsewhere.^{9,14} The structure is shown in Fig. 1(a). Additionally, in order to contrast the presence of 2DEG and for obtaining the dielectric function (DF) of thin Cu film alone, a second set of reference samples were prepared as shown in Fig. 1(b). Two other samples, Si/SiO₂ and Si/SiO₂/Bi₂O₃ were made in order to measure the SiO₂ film thickness of all samples' common substrate, and to determine the dielectric function of Bi₂O₃ in the present spectral range.

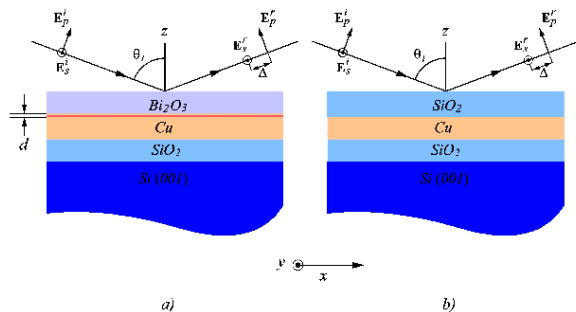


FIG. 1. (Color online) Diagrams of the samples used for the ellipsometry measurements at angles of incidence θ_i . (a) Main samples Si(001)/SiO₂/Cu/Bi₂O₃ (Cu thicknesses are 10, 20, or 50 nm). The 2DEG formed upon deposition of the Bi₂O₃ film is depicted with thickness d . (b) reference sample with SiO₂ instead of Bi₂O₃. x , y and z are the axes for which the tensorial complex components $\varepsilon_{xx} = \varepsilon_{yy}$ and ε_{zz} of the 2DEG are related. E_p and E_s stand for p and s polarizations for both incident and reflected optical electric fields, and Δ is a measure for the retardance between p and s polarizations upon reflection. See text for details.

The samples were characterized by infrared spectro-

scopic ellipsometry (IRSE) by means of an IR-VASE apparatus (J.A. Woollam Co.). Ellipsometry measures the change in polarization state upon oblique reflection of an originally linear polarized incident beam.¹⁵ The reflected state of polarization is measured by the complex ratio

$$r_p/r_s = \tan \psi \exp(i\Delta), \quad (1)$$

where r_p and r_s are the complex reflection coefficients for p and s polarizations of light, standing for parallel and perpendicular to the plane of incidence, respectively. The ellipsometric angles ψ and Δ measure then the relative change of amplitude and phase, respectively, of the p to s polarizations.¹⁶ Mid-infrared SE (spectroscopic ellipsometry) was measured in the range of ~ 35 to 760 meV in ambient conditions for angles of incidence $\theta_i = 35^\circ, 45^\circ, \dots, 85^\circ$. As the indicatrix of an uniaxial material is oriented with its distinct axis perpendicular to the sample surface, i.e., $\varepsilon_1 = \varepsilon_2 \neq \varepsilon_3 (= \varepsilon_z)$ an ordinary so-called isotropic-like ellipsometry measurement is sufficient to fully characterize the optical properties.¹⁷ Neither off-diagonal Jones matrix elements nor Müller matrix measurements provided further information for our samples.

For the mid-infrared studies, where silicon is transparent, partially incoherent light reflected off the backside surface can reach the detector. Thus the backside of the samples were subjected to a sand-blasting treatment, obtaining thus a surface rough enough so as to avoid specular, spurious reflection from it. The success of the treatment is tested by transmission and depolarization measurements, which are acquired with the same ellipsometer. Transmission turned out to be negligible for all samples, whereas the loss of polarization yielded near zero values as well, except for samples with thicker Cu film and only for $\theta_i = 85^\circ$, for which the loss is below 2.5%. This may indicate another source of depolarization. Resulting experimental spectra are shown with symbols in Fig. 2.

III. ELLIPSOMETRY MODEL

In this section we describe the procedure to obtain the model employed in the present work for the diagonal, uniaxial, dielectric tensor representing the optical response of the 2DEG. We present first the model of stacked layers and the dielectric functions of the corresponding constituent materials followed by the 2DEG dielectric tensor. The model the 2DEG layer is stripped to the minimum number of oscillators that permitted a good fit. We note that the core result of this work, shown in Fig. 2, presents some deviations from experiment which might have been corrected by including more oscillators, however, this is avoided if a physical interpretation cannot be provided.

The layer basic constituents' dielectric functions, i.e., those of Si, SiO₂, the thickness dependent Cu, and Bi₂O₃, were obtained either from literature or extracted from

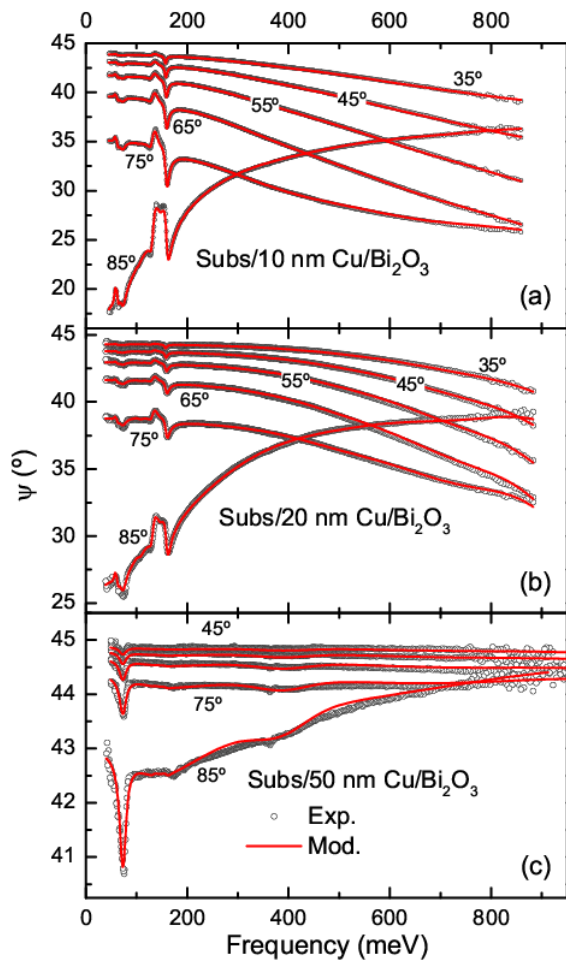


FIG. 2. (Color online) Experimental (symbols) and calculated (lines) ψ spectra recorded at different angles of incidence (indicated) corresponding to Bi_2O_3 on (a) 10 nm Cu, (b) 20 nm, and (c) 50 nm Cu layers, respectively.

reference samples, so that for the main $\text{Cu}/\text{Bi}_2\text{O}_3$ samples, the only *permitted* unknown is the 2DEG response. Moreover, spectra corresponding to all angles of incidence are fitted together employing the same constituents. This ensures consistency of the model.

A. Constituent materials

The total reflection coefficients¹⁸ in Eq. (1) are calculated separately for s and p polarizations using Fresnel coefficients consisting of, for the main $\text{Cu}/\text{Bi}_2\text{O}_3$ samples, a model of 6 stacked media: (0) vacuum, (1) 20 nm Bi_2O_3 , (2) an interfacial, anisotropic layer to accommodate the 2DEG, (3) Cu thin film, (4) 320 nm SiO_2 , and (5) Si substrate [see Fig. 1(a)]. Similar models are used for the different reference samples, for instance, Fig. 1(b) corresponds to $\text{Si}/\text{SiO}_2/\text{Cu}/\text{SiO}_2$. It is important to note that attempts made to model the $\text{Cu}/\text{Bi}_2\text{O}_3$ spectra without the artificially introduced 2DEG layer failed

to simulate the main features of the experimental curves as presented in Fig. 3(a). However, it worked nicely for the Cu/SiO_2 reference samples, as shown in Fig. 3(b), indicating that the interfacial layer must be necessarily included in the description of the optical response of the $\text{Cu}/\text{Bi}_2\text{O}_3$ system.

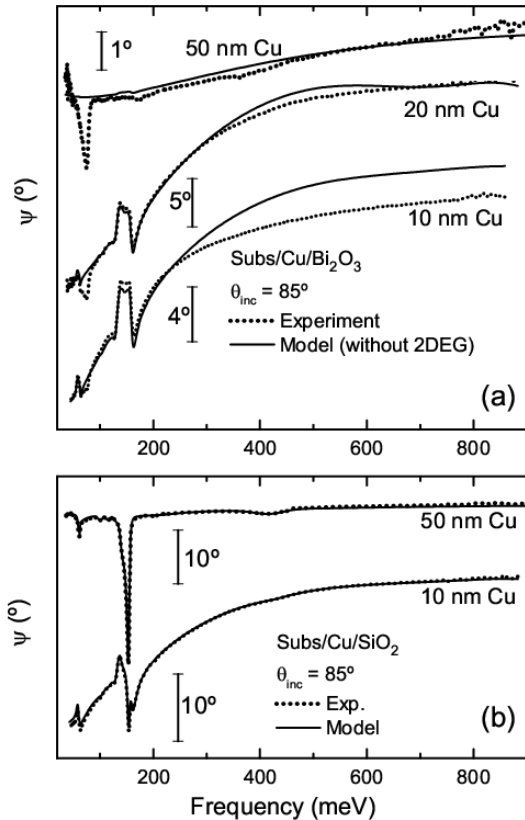


FIG. 3. Calculated (solid lines) and experimental (dashed lines) ψ spectra at an angle of incidence of 85° corresponding to (a) the main samples, Subs./Cu/ Bi_2O_3 for the indicated Cu thicknesses, for which a 2DEG interfacial layer is not included. These are to be considered the starting point of the modeling. (b) Spectra of Subs./Cu/ SiO_2 -type reference samples. This kind of samples are used to determine the Cu thickness-dependent optical conductivities presented in Fig. 4(c). In both, the vertical scales correspond to units of ellipsometric angle ψ : each spectrum is scaled differently to aid visualization.

In order to ensure Kramers-Kronig consistency, the complex dielectric function of each layer is parameterized as a sum of oscillators of a general form

$$\varepsilon(\omega) = \varepsilon_\infty + \varepsilon_D(\omega) + \varepsilon_{TL}(\omega) + \sum_i \varepsilon_{L,i}(\omega), \quad (2)$$

where ε_∞ is a (real) constant offset, the $\varepsilon_{L,i}(\omega)$ terms are used to include resonances within the measured spectral range, commonly Lorentz or complex Gaussian functions. ε_{TL} is the Tauc-Lorentz oscillator,¹⁹ which is used here because of its pulse-like shape as described below. The $\varepsilon_D(\omega)$ term corresponds to the classical Drude model for

free carriers expressed through

$$\varepsilon_D(\omega) = -\frac{\sigma^0}{\varepsilon_0\omega(i + \tau\omega)}, \quad (3)$$

where the offset with which this equation is commonly written is passed to ε_∞ in Eq. (2), and σ^0 is the DC conductivity, which, for the case of the interfacial 2DEG, will be replaced by the appropriate tensorial component σ_{ij}^0 . Similarly, in this layer the characteristic life time τ will be direction dependent, as well. However, if the material of the layer is around the percolation threshold, the Drude term can be replaced by a Drude-Smith line shape given by²⁰

$$\varepsilon_{DS}(\omega) = \frac{i}{\varepsilon_0\omega} \frac{\sigma^0}{1 - i\omega\tau} \left(1 + \frac{c}{1 - i\omega\tau} \right) \quad (4)$$

which accounts for stochastic persistency of velocity of carriers after scattering events measured through the factor c ($-1 < c < 0$). In this model τ will be the average collision time, and thus the real DC conductivity, i.e., the one obtained by extrapolation to $\omega \rightarrow 0$ is reduced with respect to that of the pristine material. The Drude-Smith model predicts a shift of spectral weight which is expressed by a broad peak in the mid-infrared region²⁰ in agreement with classical percolation theories.²¹ The required Lorentzian and Tauc-Lorentz oscillators are only phenomenological descriptions for the physical reality of the spin-orbit coupling⁸ related bands and inter-subband transitions that serve to place experimentally those resonances.

The dielectric function of α -Bi₂O₃ was extracted from a Si/thermal SiO₂/Bi₂O₃ reference sample. To this end a reference substrate Si/SiO₂ was fitted first. The thermal SiO₂ dielectric function was taken from data sets without modifications. It is shown in Fig. 4(b) (dashed line). The resulting complex dielectric function ε of Bi₂O₃ is shown in Fig. 4(a).

Employment of Si/SiO₂/Cu/SiO₂ reference samples was required to extract the thickness dependent Cu dielectric function, since in this samples no 2DEG formation is expected. Due to the preparation method, i.e., evaporation instead of thermal formation, the dielectric function of the most external SiO₂ layer did require some modification. Its ε resembles more that of a bulk glass (a microscope slide). In Fig. 4(b) we show the spectral region where the preparation-dependent differences are stronger.²²

For the present Cu thin layers, the bulk dielectric function cannot be used since for these thicknesses the Cu layers are still near the mentioned percolation threshold²³⁻²⁵ even though they are already continuous. The layers of 20 and 50 nm required the classical Drude model only, however, for the 10 nm Cu film the Drude-Smith correction was necessary to better fit the Cu/SiO₂ data of Fig. 3(a), since the model without the correction had the tendency of rising above the experimental data at the lower end of the spectrum. The resulting Cu optical con-

ductivities are shown in Fig. 4(c), where bulk data²⁶ are shown for comparison.

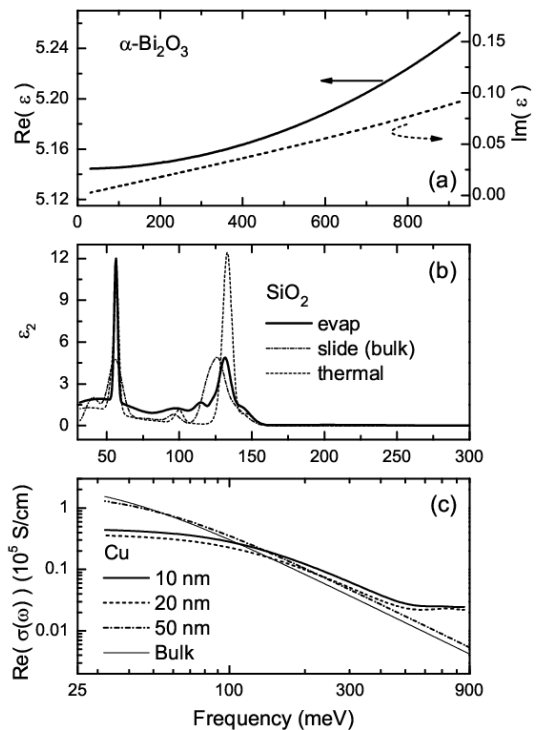


FIG. 4. Dielectric functions (or optical conductivities) of the basic constituents of the optical model. (a) Complex dielectric function of α -Bi₂O₃ as obtained from a reference sample. (b) ε_2 of SiO₂. The labels *evap* and *thermal* correspond to the evaporated layer for reference samples with no 2DEG formation, and the substrate for all samples in the present work, respectively. *slide (bulk)*, is presented for comparison. Notice the shorter spectral range used to emphasize the region of SiO₂ characteristic vibrations. The SiO₂ reference samples (see Fig. 3) were employed to extract the Cu thickness-dependent optical conductivities depicted in (c). Cu bulk data were taken from Ref. [26] for guidance.

B. Anisotropic model for the 2DEG

The 2DEG layer has drastically different transport properties along the Cu/Bi₂O₃ interface and perpendicular to it. This strong disparity prompted us to pursue a simulation-to-experiment approach instead of the common experiment-to-theory procedure. To extract its frequency dependent tensorial complex components $\varepsilon_{xx} = \varepsilon_{yy}$ and ε_{zz} , we first proceeded with the assumptions that the conductivity along the interface is much greater than that of the out-of-plane component, and that a forced isotropic approximation could suffice to provide a preliminar lineshape as a first approximation, and thus, learn already something about the main spectral features as described next. A similar anisotropic approach has been conducted for perovskites characterized

also by infrared ellipsometry²⁷ in which a Berreman resonance is excited by the presence of a longitudinal phonon in one of their constituents. In our case, on the other hand, the properties of the out-of-plane conductivity, in particular a sort of “bulk” plasmon-like characteristic frequency, and not a longitudinal phonon, are critical for the description of the present experiments as discussed in the following.

The extracted “isotropic” optical properties are to be considered a pseudo dielectric function $\langle \varepsilon \rangle$ of the layer: from a set of pre-simulations we first inferred that $\langle \varepsilon \rangle \neq \varepsilon_{ij} \ell_i \ell_j$ (the modulus of a tensor along a given direction) even for bulk-like transparent well-oriented uniaxial media, where $i, j = (x, y, z)$ and ℓ_i are direction cosines of the traveling electric displacement vector \mathbf{D} . This implies that, as we learned from simulations, in the case of free electron behavior described by Drude line shape of the form (ρ_0, τ) , where ρ_0 is the dc resistivity and τ is the characteristic time of life, that when the dc parts of the optical conductivity moduli follow the relation $\sigma_{xx}^0 > \sigma_{zz}^0$ the isotropically forced conductivity $\langle \sigma \rangle$ tends to overestimate the dc σ_x component even by an order of magnitude. However, the isotropic-like time of life τ_{iso} turns out to be τ_x along the interface, and tends to be always correctly predicted at least under the aforementioned dc conductivities relation. Interestingly, the bulk plasmon frequency ω_p ; i.e., the crossing $\text{Re} \varepsilon(\omega_p) = 0$, produces a resonant-like feature in ellipsometry spectra where there is no actual resonance. In fact, for the isotropic forced simulation, this peak was simulated with a Fano resonance due to its asymmetric form,^{28,29} which can be seen more clearly in the experimental spectrum at $\theta_i = 85^\circ$ in Fig. 2(c), and was even seriously considered as a candidate to be a contribution of either ε_{xx} or ε_{zz} were not for the simpler explanation provided by the out-of-plane conductivity. Moreover, attempts to introduce a Fano resonance resulted in non physically negative dielectric functions. Therefore, any simulation taking into account Fano resonances was excluded in the anisotropic model. The asymmetric negative peak was thus obtained in simulations as follows: the feature is quite pronounced in calculated spectra of bulk-like samples if any one of ε_x and/or ε_z has this crossing, but for films on Cu substrates this apparent resonant feature is only revealed in calculated ellipsometry spectra for the ε_z crossing and not for ε_x even if this last function has it. We can therefore regard the presence of this feature, as the one at around 70 - 80 meV in Fig. 2, as a signature of the formation of an anisotropic layer at the Cu/Bi₂O₃ interface, which in our case is extremely revealing since our samples are composed of amorphous materials and therefore have isotropic dielectric functions. To sustain this proposition we note that (i) this is not a SiO₂ vibration: the frequencies do not exactly correspond and for the sample with thicker Cu layer, as seen in Fig. 2(c), Cu clearly quenches any SiO₂ feature, but the ε_z crossing related peak is very dominant. (ii) This feature should not be confused with a Berreman peak³⁰ or other similar peak-like features, since

those occur either close to actual resonances,³⁰ when the substrate has a crossing³¹ $\text{Re} \varepsilon = 1$ with positive slope (and not $\text{Re} \varepsilon = 0$, as in our case), or when the real part of the dielectric functions at both sides of the interface coincide,^{32,33} respectively. We clearly have not the conditions to fulfill any of these criteria.

For Lorentz or Gaussian line shapes, as the ones assigned to spin-orbit coupling bands in the next section, simulations showed that both characteristic centers and broadenings can be already correctly inferred from isotropic-like simulations. The real parts $(\text{Re} \varepsilon_L)_x$ and $(\text{Re} \varepsilon_L)_z$, which describe the elastic response of the media, are inverted with respect to each other. For layered media, the real and imaginary parts seem to be interchanged in the total ellipsometry spectra. All these criteria provide guidance to decide whether a feature is to be part of the x or z component of the ε tensor, based also on reduction of fitting error.

Concerning film thicknesses, the forced isotropic “best” fit also overestimates film thicknesses of the supposed 2DEG layer. The obtained artificial layer thickness forming between Cu and Bi₂O₃ resulted in 2 to 3.6 nm depending on the underlying Cu film thickness for the forced-isotropic model, whereas for the more realistic uniaxial model, the thicknesses are all between 0.5 and ≤ 1 nm (see Table. I, below).

Finally, for the 2DEG optical properties we propose the following description: the two-dimensional character of the electron gas will be described through a very thin layer with dielectric function of tensorial, uniaxial character, for which the carrier transport is much easier along the interface. The in-plane tensor modulus ε_{xx} will have a Drude (or Drude-Smith) component to accommodate the free electron contribution to the 2DEG, and two Gaussian oscillators to simulate the SOC contributions.⁸ The out-of-plane ε_{zz} modulus will be comprised of a free electron Drude contribution, for which the relation $\sigma_{zz}^0 \ll \sigma_{xx}^0$ holds, but which is nevertheless finite in such a way that it has a “bulk” plasmon $\text{Re} \varepsilon_{zz}(\omega_{p,z}) = 0$ crossing, which is critical in our model. Additionally, ε_{zz} includes a Tauc-Lorentz oscillator whose role, expected by theoretical considerations,⁸ will be described in the next section. The model as such is simple as desired, and quite descriptive of the actual experiments as seen in Fig. 2. Each spectral feature is modeled with two (for the classical Drude) to four parameters (for the percolation modified Drude-Smith model), which apparently amount to a large number of free quantities to be determined, however, most of the spectral features are well separated from the rest and can be thus considered as independent from the others. Furthermore, the isotropic-forced first approach already provides a good estimation of the values of some of them, specifically, the in-plane free-electron life time and positions of both SOC peaks. Additionally, the correlation between some parameters, and its possible source, is discussed at the end of the main text.

IV. RESULTS AND DISCUSSION

The substrate Si/SiO₂, and the Si/SiO₂/Bi₂O₃ reference samples were fitted with VASE32, obtaining thus the thickness of the thermally grown SiO₂ of 322 nm, and the mid-infrared *pristine* Bi₂O₃ dielectric function of Fig. 4(a), which are used for all subsequent samples. α -Bi₂O₃ has a series of small phonons in this spectral region below 66 meV,^{34,35} which were not detected in our experiment. Also, the group of features at ~ 60 and 150 meV in Fig. 2(a), (b), and Fig. 3(a),(b) correspond to SiO₂ and their strengths, when SiO₂ is used only as the substrate of Cu/Bi₂O₃, can therefore be employed as a gauge of spectral absorption by the different Cu layers. For the SiO₂/Cu/SiO₂ reference spectra, shown in Fig. 3, the dips are easily reproduced by the proper model without great effort.

Experimental and calculated ψ spectra for the different Cu/Bi₂O₃ samples recorded at several angles of incidence are shown in Fig. 2(a)-(c). The overall spectra are dominated by Cu reflectivity and its corresponding thickness-dependent optical conductivity $\sigma(\omega) = i\omega\epsilon_0(1 - \epsilon(\omega))$. The resulting tensorial dielectric complex moduli, ϵ_{xx} and ϵ_{zz} of the 2DEG forming at the Cu/Bi₂O₃ interface are presented in Fig. 5. The resulting dielectric properties depend on the underlying Cu film thickness-driven transport properties. This dependence can be explained in terms of modulation of charge transfer from Cu to Bi₂O₃ due to the mobility of electrons within the Cu layer itself: for thicknesses below 20 nm the layer is below its percolation threshold (in fact, 10 nm Cu was modeled with the Drude-Smith approach), which implies the formation of potential barriers within the Cu layer; very likely produced by plane defects at the domain connections, and consequently modified work functions. Indeed, it has been reported that the relation of work functions of the materials at the interface is critical for its resulting characteristics, like the relative occupancy of hybridized orbitals near the interface,³² and thus, those of the 2DEG at the Bi₂O₃ on non-magnetic metals interfaces¹¹ and perovskite oxide-oxide interfaces, as well.⁶

The new layer, in contrast to the aforementioned Cu/SiO₂ experiments, resulted in strong optical spectral features quite different from those of the original constituent materials as evinced by comparing Fig. 5 and Figs. 4(a) and (c). Strikingly, the line shape of the interfacial layer DF thus resolved in Drude and other resonant oscillator components, resulted very similar to theoretical predictions⁸ of a two dimensional electron gas confined in the normal direction of the system. The hybridization of interfacial orbital states induce electronic asymmetric wave functions and splitting of spin-orbitals, in contrast with the original constituent materials which do not possess SOC. Such asymmetric wave functions thus induce an interfacial electric field suggesting SOC of the Rashba type.^{36,37} This statement is in agreement with first-principle calculations recently reported for Cu/Bi₂O₃.^{11,38}

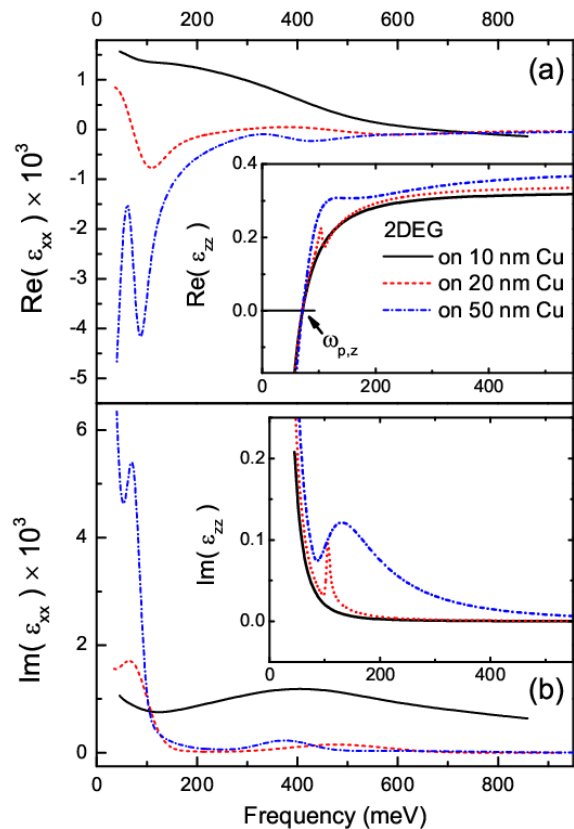


FIG. 5. (Color online) Real (a) and imaginary (b) parts of the diagonal dielectric tensor components of the 2DEG interfacial layer forming between Bi₂O₃ and Cu as extracted from the fitting procedure for the samples with Cu layer thickness of 10, 20, and 50 nm, as indicated. The main plots show ϵ_{xx} and the insets correspond to ϵ_{zz} . The plasmon frequency $\omega_{p,z}$ is indicated with a horizontal line at the crossing $\text{Re}(\epsilon_{zz}) = 0$.

As mentioned above, the 2DEG ϵ_{xx} and ϵ_{zz} moduli are very different. The scales in Fig. 5 differ by four orders of magnitude between x and z components and the spectral structures are very dissimilar. Had we kept an isotropic approach for all layers, the fitting error would grow with increasing angle of incidence. This error, although present, is misleadingly small and could have been easily considered as random instead of systematic. The 2DEG anisotropic dielectric functions in Fig. 5 are dominated by the free electron contribution, which is modeled by a classic Drude line shape for the 20 and 50 nm Cu samples. The 2DEG free electron part corresponding to the 10 nm Cu sample was simulated with the Drude-Smith approach.²⁰ The broad spectral structure centered at ~ 400 meV is then a sign of abundance of scattering events, and is consistent then, with phenomenological percolation theories producing a mid-infrared broad peak accompanying the main Drude feature, and predict a recovery of the usual free-electron gas behavior as the percolation threshold is surpassed.²⁰ For perovskites systems this metal-insulator transition has been studied as a function of temperature and by modu-

lating carrier densities by means of gating.^{39,40} Here, the carrier density and the Rashba effect-inducing interfacial electric field are provided by the dielectric characteristics of the underlying Cu supporting film. The parameters, such as dc conductivities σ_{xx}^0 , σ_{zz}^0 , and mean times of life τ_{xx} and τ_{zz} of the free electron contribution to the 2DEG are presented in Table I as functions of underlying Cu film thickness. It is observed that while σ_{xx}^0 increases non monotonically, but fast with increasing Cu thickness, it does not show a clear one-to-one relation with the corresponding Cu-depending dc conductivity. Furthermore, τ_{xx} also increases as a function of underlying Cu thickness, but it is quite different than the time of life of its conducting support. This is a critical argument in favor of a forming 2DEG interfacial layer: it will be shown below, in the context of Fig. 7, that an independent time of life cannot be achieved for an arbitrarily introduced artificial layer. Also, the non monotonic increment of τ_{xx} can be associated to an additional interfacial build-up strain⁴¹ possibly induced by different densities of oxygen vacancies of Bi₂O₃ at the interface, as it happens in the STO/LTO crystalline or amorphous systems.^{7,42}

In Table I we also report on the thickness of the 2DEG layer, d . This number provided minimization of error in the present interface anisotropic model, however, this does not preclude some (fast decaying) extension of the effect further in z -direction as observed in Ref. [33]. Furthermore, since the Bi₂O₃ layer is already very thick, 20 nm, the explanation for the non monotonic variation in 2DEG thickness is not expected to be related to number of Bi₂O₃ monolayers,³² but more likely due to the transition to free-like (for the 20 nm Cu sample) from collision-rich (for the 10 nm Cu sample) transport along the interface.

The rest of the most relevant 2DEG interfacial layer spectral features in Fig. 5 are presented next. Since the two ε_{xx} resonances at around 80 and 400 meV, as extracted from calculation, are consistent with theoretical predictions⁸ concerning their relative amplitudes, frequency positions, and the behavior of their frequency-shifts and strengths as a function of (Cu-provided) charge density, we will regard them as (low frequency) SOC₁ and (high-frequency) SOC₂, respectively. They are shown separated from the rest of the contributions in Fig. 6.

The orbital hybridization allowed⁸ SOC₁ resonance (near the vertical marker in Fig. 6), notably increases in strength as function of available charge in the interfacial layer, whereas its shifting position (to higher frequencies) seems to come to a stop for underlying Cu thickness above 20 nm. At higher frequencies, the structure assigned as SOC₂, is detected only for the thicker Cu samples. It notably shifts to lower frequencies, in opposition to SOC₁, and its strength slightly increases with increasing carrier density. The behavior of amplitude ratios, broadening, and energy positions of SOC₂ and SOC₁ in Fig 6, are quite consistent with the trend predicted for intersubbands optical response as a function of carrier density at the 2DEG.⁸

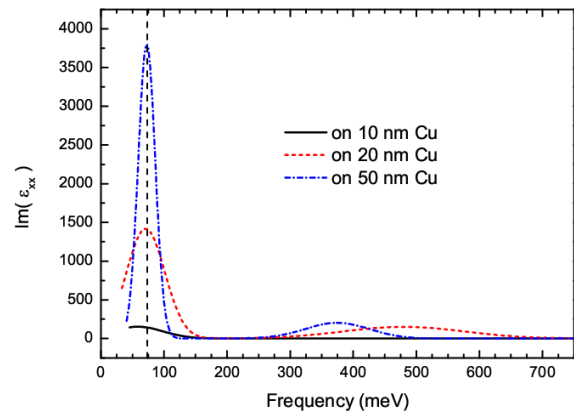


FIG. 6. (Color online) Imaginary part of the Rashba-enabled spin-orbit coupling (SOC) contributions to the total 2DEG dielectric function shown in Fig. 5, corresponding to the indicated thickness of the Cu underlayer. The obtained spectral positions, widths and amplitudes depend on the 2DEG charge density in fair agreement with theory.⁸

The out-of-plane 2DEG dielectric functions ε_{zz} , in spite of their smallness produce dramatic features in the ellipsometry ψ spectra, the main one is the already discussed sharp, asymmetric peak at ~ 75 meV resulting from the crossing $\text{Re } \varepsilon(\omega_{p,z}) = 0$. As seen in the inset of Fig. 5(a), the position of this crossing, which consists of an interplay of particular values σ_{zz}^0 and τ_{zz} , seems to be quite general for the Cu/Bi₂O₃ system, whereas the slope is sensitive but only slightly to the actual properties of the charge density. Moreover, a really similar feature is also seen in the Ag/Bi₂O₃ system (this will be presented elsewhere), which might hint to a stark influence of Bi-O orbitals on the properties of the 2DEG,^{9,10} and could be interpreted in the light of a surface-orbital Rashba effect.⁴³ A second feature in ε_{zz} at ~ 100 – 200 meV (see insets in Fig. 5), which was revealed during the iterative procedure described above, was simulated with a Tauc-Lorentz oscillator due to its pulse-like form. This feature in ε_{zz} is also consistent with theory, however, the resolution of our model only provided a spectrum resembling the envelope of the z -conductivity of Ref. [8]. Thermal effects and inherent instrument signal to noise do not permit to resolve subband transitions, thus we cannot infer whether they are present in the Cu/Bi₂O₃ system or not as in the perovskite calculations.

Some apparent discrepancies of our results with theory,⁸ besides of the obvious differences between systems, might be explained by the actual condition of realistic samples. First, the near percolation threshold conductivity of the 10 nm thick underlying Cu sample imposes its character to the corresponding 2DEG conductivity. Actually the 2DEG free-electron contribution exhibits more collisions-related characteristic conductivity than its underlying Cu. The concomitant spectral weight shift to mid-infrared makes its $\text{Im}[\varepsilon_{xx}]$ to look higher than the spectra of the other samples [see Fig. 5(b)], while the

TABLE I. Relevant parameters of the interfacial 2DEG layer depending on underlying Cu thickness t_{Cu} . d is the 2DEG thickness, σ_{ij}^0 and $\tau_{i,j}$ are the DC conductivity and relaxation lifetimes of the in-plane and out-of-plane Drude contributions, respectively. ω_i and γ_i ($i = (1, 2)$) are SOC $_i$ peaks center and broadening, respectively.

t_{Cu} (nm)	d (nm)	Free-electron				SOC $_1$		SOC $_2$	
		σ_{xx}^0 (10^3 S/cm)	τ_{xx} (fs)	σ_{zz}^0 (S/cm)	τ_{zz} (fs)	ω_1 (meV)	γ_1 (meV)	ω_2 (meV)	γ_2 (meV)
10	0.59 ± 0.01	5.0 ± 0.01	1.6 ± 0.002	18.2 ± 0.001	53 ± 0.8	55 ± 10	99 ± 18	–	–
20	0.53 ± 0.02	4.5 ± 0.9	9.0 ± 1.8	16.0 ± 0.3	42 ± 0.8	71 ± 4	70 ± 3	480 ± 6	226 ± 3
50	0.82 ± 0.005	11.7 ± 2.5	18.2 ± 3.6	15.8 ± 1.2	28 ± 2.2	69 ± 14	30 ± 6	360 ± 14	170 ± 20

real parts reflect a more orderly trend. Also the dc conductivities follow a nice trend (see Table I). Second, the SOC features in Fig. 6 are fairly consistent with theory, but show some differences: SOC $_1$ grows with charge density but does not shift in frequency when comparing 20 and 50 nm Cu samples, and SOC $_2$, although it presents the correct shift, it does not grow noticeably when comparing those same samples. This can be explained by the presence of oxygen vacancies,⁴⁴ which are critical for the acceptance of carriers from the underlying layer in perovskite^{7,42} and Bi $_2$ O $_3$ systems,⁴⁵ and might very well be also relevant in the present Cu/Bi $_2$ O $_3$ system. These vacancies also produce a strain field in their vicinity and might influence how the orbitals finally hybridize near the interface, allowing thus for the contrasting properties of Bi $_2$ O $_3$ near the Cu interface with respect to the Bi $_2$ O $_3$ energy structure in the bulk.⁴⁶

A further utilization of the SiO $_2$ /Cu/SiO $_2$ reference samples consisted on trying to emulate artificially the presence of a 2DEG-like intermediate layer in order to verify whether the Cu/Bi $_2$ O $_3$ interface model was real or an artifact: In Cu/SiO $_2$ the artificial layer dielectric function, simulated with the isotropic-forced model, and once parameterized with oscillators of the underlying Cu and SiO $_2$, resulted on an effective medium-like combination of both, depending on the layer placement as shown in the inset of Fig. 7. In all the instances described below, the calculated ψ spectra reproduce faithfully the experimental curves. The artificially introduced layer presents, dominantly, characteristics of a conducting material of different dc conductivities as seen by the varying heights of the crossing points of the Ordal analysis⁴⁷ in Fig. 7(a), but the frequency of the interceptions, which is directly related⁴⁷ to the characteristic τ is always preserved and equal to the one of the underlying Cu. Fig. 7(b) shows energy derivatives of the real part of the artificial interface's dielectric function, which is also sensitive to changes of τ : parallel spectra confirm that τ is preserved. The reason for showing derivative spectra plots is that they tend to enhance spectral structures, and thus show that SiO $_2$ signals are growing when fraction of artificial layer depth is more to the side of SiO $_2$. Furthermore, the fact that the derivative spectra run parallel for the different artificial layer placements indicates that no other spectral peaks or “special features” can be unintentionally obtained by introducing a non-existent layer. The preservation of char-

acteristic τ in the artificial layer is in clear contrast to the results of Cu/Bi $_2$ O $_3$ interface model, which produced τ_{xx} values different from the one of the underlying Cu.

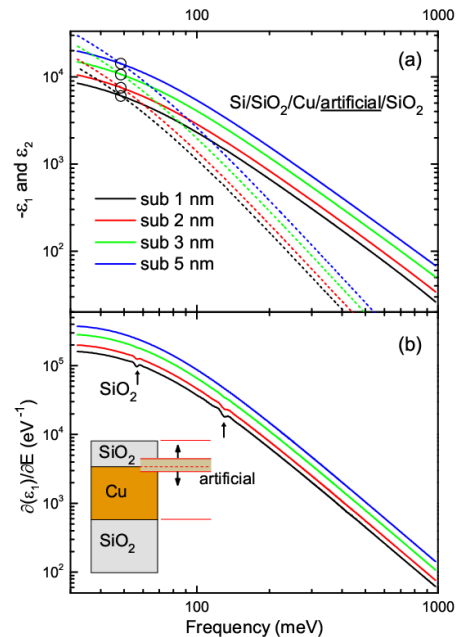


FIG. 7. (Color online) Test simulations of a falsely assumed 2DEG-like layer forming at the Cu/SiO $_2$ interface for the reference samples following the scheme in the inset. The artificial layer is placed at different depths measured from the actual interface as shown in the scheme. The Ordal-type analysis $-\epsilon_1$ vs ϵ_2 (solid and dashed lines, respectively) in (a) for the thus artificially introduced layer indicates, by the intersections (see the large circles), that the characteristic time of life is the same for all layer depths. This is confirmed by the equal curvatures of the energy-derivative of ϵ_1 in (b).

Motivated by the closeness of a large Cu $_2$ O IR-active phonon to the sharp experimental feature at ~ 76 meV, in Fig. 8 we present simulations of spectra corresponding to 50 nm Cu/Bi $_2$ O $_3$ in which the interfacial layer has been substituted by a medium consisting of a mixture of Cu $_2$ O and Cu. The simulations reproduce reasonably well the ψ heights, but with unrealistic layer thicknesses of the basic constituents which are at odds with our TEM measurements (a separate manuscript is in preparation). The Cu $_2$ O+Cu layer is also very thick as shown in Fig. 8(a) and (b). The rationale behind the introduction of Cu in

this layer is to provide it of conducting properties. However higher Cu volume fractions also quenched the Cu_2O peak.

Other features which cannot be reproduced by these layers include e.g., the SOC_2 broad peak, which is highlighted in gray in Fig. 8. Although the bulk Cu_2O feature has been ruled out in our model, we cannot neglect Cu-O bonding at the interface, which is critical for the interfacial final orbital hybridization states. The issue here is that its features are either out of working range or below our detection limit. In fact, we did not detect any of the reported⁴⁸ Cu oxides by separate confocal Raman studies. In the case of perovskites, it has been shown that some metals are reactive upon deposition, in particular the oxidation of Al contributes extensively to the presence of oxygen vacancies at the SrTiO_3 (STO) side, and thus of 2DEG formation,⁴⁹ which shows very large spin-charge interconversion efficiencies.⁵⁰ It is also known that Cu has poor reactivity to the oxide STO.⁴⁹ From this, we might assume that in the $\text{Cu}/\text{Bi}_2\text{O}_3$ system, Cu will also present poor reactivity, thus, the dependence of the transport properties with the Cu thickness cannot be explained by oxidation of the metal, but by the thickness-dependent conducting properties of the support itself.

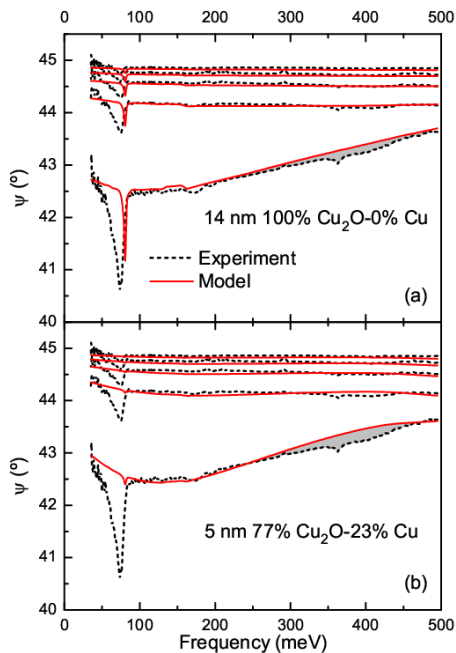


FIG. 8. (Color online) Test simulation for the 50 nm $\text{Cu}/\text{Bi}_2\text{O}_3$ sample. The 2DEG layer is replaced by an effective medium comprised of Cu_2O and Cu. While the overall ψ values are well reproduced for the indicated film thicknesses and proportions, obvious discrepancies are noted, specifically, the lack of SOC_2 indicated by the gray shaded area, and the failure to reproduce the low frequency side of the experiment due to the absence of both, SOC_1 and the ε_{zz} crossing effect.

In Fig. 9 we present a study of errors induced in the calculation by removing some features whose frequencies are very close together in the range of 10 to 130 meV, for

which analytic oscillator functions (in the sense of “in opposition to numerical data”) were continued below the experimental range (initial frequencies are 30 – 40 meV, depending on light availability) in order to discard the influence of undesired features out of the working spectral range. We compare the final result of Fig. 2(b) for the 45° angle of incidence, which has a significant projection of x component of incident p electric field, to several situations.

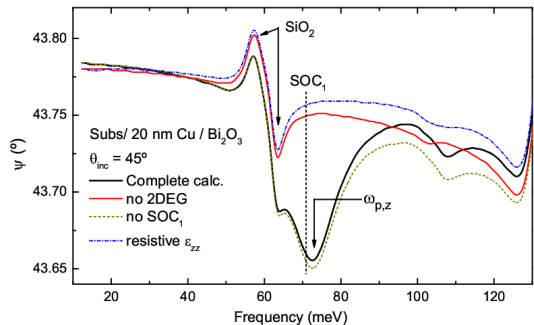


FIG. 9. (Color online) Calculated ψ spectra for the 20 nm $\text{Cu}/\text{Bi}_2\text{O}_3$ sample for which several features are removed separately, including the complete 2DEG layer, in order to observe their influences in the spectral region around 70 meV.

The complete removal of the 2DEG layer, which also induces an error due to film thickness, provides an idea of our starting point. This spectrum reveals that the Cu dielectric function and thickness, as extracted from reference samples, are appropriate for the $\text{Cu}/\text{Bi}_2\text{O}_3$ system, since the SiO_2 features in this range seem fairly correct concerning size and phase of the feature. The influence of the conducting part of the z -component is seen by simulating the 2DEG layer with a ε_{zz} of resistive character, which therefore lacks the $\omega_{p,z}$ crossing. We conclude that its presence is the most significant contribution for the ~ 72 meV negative peak in ψ . The subbands feature of ε_{zz} also helps to correctly place a small kink at ~ 110 meV. Its presence in experiment is more clearly seen in the $\theta_{\text{inc}} = 85^\circ$ spectrum in Fig. 2(b). In this series of simulations we also removed the oscillator corresponding to SOC_1 . In Fig. 9 we have indicated the center of this resonance with the vertical line. Calculations show that the real part of the oscillator for this layer has more influence in ψ , whereas its peak-like imaginary part contributes more to refinement of Δ spectra. Fig. 9 probes that SOC_1 has a more delocalized impact on the spectrum, which is more noticeable at higher frequencies from its center. In Table I, some of the parameters show large errors, sometimes of the order of 20%. This can be attributed to high correlations among different parameters and thus a great difficulty to clearly separate contributions, in particular those present at the low frequency side of the working range. This can be illustrated, for example, by comparing in-plane conductivity parameters: the Drude characteristics σ_{xx}^0 and τ_{xx} for the 20 nm and 50 nm Cu samples present large errors

partly due to the featureless character of the classical Drude line shape which can be contrasted to the 10 nm Cu sample resulting parameters, which show nearly negligible uncertainties, possibly since its percolation-related mid infrared peak allows for an easier deconvolution. In the case of the SOC₁, the difficulty to be extracted and its concomitant error are very likely consequence of its non-local influence on the overall spectrum as mentioned above, in Fig. 9.

V. CONCLUSIONS

In summary, we have detected the presence of a 2DEG at the interface of an amorphous oxide with a non magnetic metal by means of infrared ellipsometry. We have found that a diagonal, uniaxial dielectric tensor of the 2DEG layer describes really well the experimental results. Furthermore, beside the substrate dependent carrier density free-electron (Drude-like) behavior, we have also observed intersubband features consistent with SOC of the Rashba type. The present report sheds light on the complex phenomena at amorphous interfaces that have been elusive for decades. This work allows, therefore, assessing the complex phenomena associated to the presence of 2DEG with SOC at interfaces between amorphous materials. Beyond the particular case of study in the present paper, the supporting theoretical model by other groups and the advanced ellipsometry technique suggests applicability in a larger range of unexplored amorphous interfaces.

ACKNOWLEDGMENTS

We thank Prof. A. H. MacDonald (University of Texas at Austin) and Prof. J. J. Palacios (Universidad Autónoma de Madrid) for insightful guidance. The expert technical support of Esequiel Ontiveros, F. Ramírez-Jacobo, and L.E. Guevara-Macías is highly appreciated. We also thank Consejo Nacional de Ciencia y Tecnología (Mexico) for Grants CB-223564-2014, CB-252867-2015, 299552 and 206298 (IRSE equipment). This work was also supported by a Grant-in-Aid for Scientific Research on Innovative Area, “Nano Spin Conversion Science” (Grant No. 26103002) and RIKEN incentive Research Project Grant No. FY2016.

Appendix: Fresnel coefficients

For clarity of how the anisotropic layer is handled in the model, we reproduce here the main equations employed to calculate the Fresnel coefficients (see e.g., Ref. [17]). The reflection coefficients at the interfaces of the 2DEG layer, which according to the layers numbered in Sec. III and Fig. 1 is layer number (2), for the case of

tensor orientation $\varepsilon_{xx} = \varepsilon_{yy} \neq \varepsilon_{zz}$ are

$$r_{12}^p = \frac{n_{2,x}n_{2,z} \cos \theta_1 - n_1 (\varepsilon_{2,z} - \varepsilon_1 \sin^2 \theta_1)^{1/2}}{n_{2,x}n_{2,z} \cos \theta_1 + n_1 (\varepsilon_{2,z} - \varepsilon_1 \sin^2 \theta_1)^{1/2}}, \quad (\text{A.1})$$

$$r_{12}^s = \frac{n_1 \cos \theta_1 - (\varepsilon_{2,x} - \varepsilon_1 \sin^2 \theta_1)^{1/2}}{n_1 \cos \theta_1 + (\varepsilon_{2,x} - \varepsilon_1 \sin^2 \theta_1)^{1/2}}, \quad (\text{A.2})$$

for the Bi₂O₃/2DEG interface, where the complex refractive index $n = \sqrt{\varepsilon}$ for nonmagnetic materials. The terms in brackets correspond to the angle of propagation within the 2DEG layer expressed in terms of the propagation angle within the Bi₂O₃ layer immediately above. These expressions are straightforwardly reduced to the isotropic case,¹⁷ so they can be used for other interfaces. For the 2DEG/Cu interface the reflection coefficients are

$$r_{23}^p = \frac{n_3 (\varepsilon_{2,z} - \varepsilon_3 \sin^2 \theta_3)^{1/2} - n_{2,x}n_{2,z} \cos \theta_2}{n_3 (\varepsilon_{2,z} - \varepsilon_3 \sin^2 \theta_3)^{1/2} + n_{2,x}n_{2,z} \cos \theta_2}, \quad (\text{A.3})$$

$$r_{23}^s = \frac{(\varepsilon_{2,x} - \varepsilon_3 \sin^2 \theta_3)^{1/2} - n_3 \cos \theta_3}{(\varepsilon_{2,x} - \varepsilon_3 \sin^2 \theta_3)^{1/2} + n_3 \cos \theta_3}. \quad (\text{A.4})$$

As the polarized light propagates through the anisotropic layer, the phase of each of its components is affected differently, and this is accounted for by using the standard model of multiple reflections through

$$\beta_2^p = \frac{2\pi d}{\lambda} \frac{n_{2,x}}{n_{2,z}} (\varepsilon_{2,z} - \varepsilon_1 \sin^2 \theta_1)^{1/2} \quad (\text{A.5})$$

$$\beta_2^s = \frac{2\pi d}{\lambda} (\varepsilon_{2,x} - \varepsilon_1 \sin^2 \theta_1)^{1/2} \quad (\text{A.6})$$

where λ is the wavelength of the incident radiation. For the isotropic layers the β phases are also isotropic.

The Fresnel coefficients are calculated for each polarization by introducing the interfacial reflection coefficients at both sides of the b -th layer, say, using the previously calculated reflection coefficients r_{ab}^i and r_{bc}^i , and the intra-layer phase shifts β_b^i , where $i = (s, p)$, by moving from bottom to top of the stacked structure¹⁸

$$r_{ab}, r_{bc}, \beta_b \rightarrow r_{abc} = \frac{r_{ab} + r_{bc} e^{-i2\beta_b}}{1 + r_{ab} r_{bc} e^{-i2\beta_b}}. \quad (\text{A.7})$$

The Fresnel coefficients are calculated in a cumulative fashion: starting with Si and SiO₂, i.e., layers 4 and 5 according to the stacked structure presented in Sec. ?? [see also Fig. 1(a)], the Fresnel coefficients r_{345}^i are calculated, then all indexes are decremented and the Fresnel coefficient r_{abc} takes the place of the previous interfacial reflection coefficient r_{bc} , i.e., r_{2345} is calculated with r_{23} and r_{345} . The process is repeated until the Fresnel coefficient of the whole stack $r_{01\dots5}$ is finally calculated. This has to be done separately for both $i = (p, s)$ polarizations. Thus, the quantities to extract, dielectric

functions and thicknesses, are included, correspondingly,

within polarization dependent reflection coefficients and β exponents.

-
- * e-mail (JMFC): jmflores@cactus.iico.uaslp.mx
 † e-mail (JP): jorgeluis.pueblanunez@riken.jp
- ¹ H. L. Stormer, D. C. Tsui, and A. C. Gossard, *Rev. Mod. Phys.* **71**, S298 (1999).
 - ² J. Mannhart and D. G. Schlom, *Science* **327**, 1607 (2010).
 - ³ H. Y. Hwang, Y. Iwasa, M. Kawasaki, B. Keimer, N. Nagaosa, and Y. Tokura, *Nature Materials* **11**, 103 (2012).
 - ⁴ C. H. P. Wen, H. C. Xu, Q. Yao, R. Peng, X. H. Niu, Q. Y. Chen, Z. T. Liu, D. Shen, Q. Song, X. Lou, et al., *Phys. Rev. Lett.* **121**, 117002 (2018).
 - ⁵ S. W. Lee, Y. Liu, J. Heo, and R. G. Gordon, *Nano Lett.* **12**, 4775 (2012).
 - ⁶ Y. Chen, F. Trier, T. Wijnands, R. J. Green, N. Gauquelin, R. Egoavil, D. V. Christensen, G. Koster, M. Huijben, N. Bovet, et al., *Nat. Mat.* **14**, 801 (2015).
 - ⁷ Z. Q. Liu, C. J. Li, W. M. Lü, X. H. Huang, Z. Huang, S. W. Zeng, X. P. Qiu, L. S. Huang, A. Annadi, J. S. Chen, et al., *Phys. Rev. X* **3**, 021010 (2013).
 - ⁸ M. Xie, G. Khalsa, and A. H. MacDonald, *Phys. Rev. B* **89**, 245417 (2014).
 - ⁹ J. Puebla, F. Auvray, M. Xu, B. Rana, A. Albouy, H. Tsai, K. Kondou, G. Tataara, and Y. Otani, *Appl. Phys. Lett.* **111**, 092402 (2017).
 - ¹⁰ M. Xu, J. Puebla, F. Auvray, B. Rana, K. Kondou, and Y. Otani, *Phys. Rev. B* **97**(18), 180301 (2018).
 - ¹¹ H. Tsai, S. Karube, K. Kondou, N. Yamaguchi, F. Ishii, and Y. Otani, *Sci. Rep.* **8**, 5564 (2018).
 - ¹² S. Manipatruni, D. E. Nikonov, and I. A. Young, *Nat. Phys.* **14**, 338 (2018).
 - ¹³ S. Manipatruni, D. E. Nikonov, C.-C. Lin, T. A. Gosavi, H. Liu, B. Prasad, Y.-L. Huang, E. Bonturim, R. Ramesh, and I. A. Young, *Nature* **565**, 35 (2019).
 - ¹⁴ F. Auvray, J. Puebla, M. Xu, B. Rana, D. Hashizume, and Y. Otani, *J Mater Sci: Mater Electron* **29**, 15664 (2018).
 - ¹⁵ R. M. A. Azzam and N. M. Bashara, *Ellipsometry and polarized light* (North-Holland, Amsterdam, 1977).
 - ¹⁶ J. Humlíček, in *Handbook of ellipsometry*, edited by H. G. Tompkins and E. A. Irene (William Andrew, Springer, New York, Heidelberg, 2005), p. 3.
 - ¹⁷ H. Fujiwara, *Spectroscopic Ellipsometry. Principles and Applications* (Wiley, England, 2007).
 - ¹⁸ O. S. Heavens, *Optical properties of thin solid films*, Dover classics of science and mathematics (Dover, New York, 1995).
 - ¹⁹ G. E. Jellison, in *Handbook of ellipsometry*, edited by H. G. Tompkins and E. A. Irene (William Andrew, Springer, New York, Heidelberg, 2005), p. 237.
 - ²⁰ N. Smith, *Phys. Rev. B* **64**, 155106 (2001).
 - ²¹ D. Stroud, *Phys. Rev. B* **19**, 1783 (1979).
 - ²² R. Kitamura, L. Pilon, and M. Jonasz, *Appl. Opt.* **46**, 8118 (2007).
 - ²³ M. Hövel, B. Gompf, and M. Dressel, *Phys. Rev. B* **81**, 035402 (2010).
 - ²⁴ H. Lee, H. Lee, J.-H. Park, H.-K. Kim, B. H. Kong, and H. K. Cho, *Jap. J. Appl. Phys.* **50**, 055805 (2011).
 - ²⁵ T. V. Amotchkina, V. Janicki, J. Sancho-Parramon, A. V. Tikhonravov, M. K. Trubetskov, and H. Zorc, *Appl. Opt.* **50**, 1453 (11).
 - ²⁶ E. D. Palik, *Handbook of Optical Constants of Solids* (Academic Press, 1985).
 - ²⁷ M. Yazdi-Rizi, P. Marsik, B. P. P. Mallet, A. Dubroka, D. V. Christensen, Y. Z. Chen, N. Pryds, and C. Bernhard, *Eur. Phys. Lett.* **113**, 47005 (2016).
 - ²⁸ U. Fano, *Phys. Rev.* **124**, 1866 (1961).
 - ²⁹ B. Luk'yanchuk, N. I. Zheludev, S. A. Maier, N. J. Halas, P. Nordlander, H. Giessen, and C. T. Chong, *Nat. Materials* **9**, 707 (2010).
 - ³⁰ B. W. Berreman, *Phys. Rev.* **130**, 2193 (1963).
 - ³¹ A. Nucara, M. Corasaniti, A. Kalaboukhov, M. Ortolani, E. Falsetti, A. Sambri, F. Miletto Granozio, F. Capitani, J.-B. Brubach, P. Roy, et al., *Phys. Rev. B* **97**, 155126 (2018).
 - ³² S. Y. Park and A. J. Millis, *Phys. Rev. B* **87**, 205145 (2013).
 - ³³ A. Dubroka, M. Rössle, K. W. Kim, V. K. Malik, L. Schultz, S. Thiel, C. W. Schneider, J. Mannhart, G. Herranz, O. Copie, et al., *Phys. Rev. Lett.* **104**, 156807 (2010).
 - ³⁴ S. N. Narang, N. D. Patel, and V. B. Kartha, *J. Mol. Struct.* **327**, 221 (1994).
 - ³⁵ A. B. Kuzmenko, E. A. Tishchenko, I. L. Sashin, M. N. Khlopkin, and V. G. Orlov, *J. Low Temp. Phys.* **105**, 861 (1996).
 - ³⁶ Y. A. Bychov and E. I. Rashba, *Pis'ma Zh. Eksp. Teor. Fiz.* **39**, 66 (1984).
 - ³⁷ A. Manchon, H. C. Koo, J. Nitta, S. M. Frolov, and R. A. Duine, *Nat. Materials* **14**, 871 (2015).
 - ³⁸ J. Puebla, F. Auvray, N. Yamaguchi, M. Xu, S. Bisri, Y. Iwasa, F. Ishii, and Y. Otani, *Phys. Rev. Lett.* **122**, 256401 (2019).
 - ³⁹ K. Ahadi and S. Stemmer, *Phys. Rev. Lett.* **118**, 236803 (2017).
 - ⁴⁰ K. Ahadi, O. F. Shoron, P. B. Marshall, E. Mikheev, and S. Stemmer, *Appl. Phys. Lett.* **110**, 062104 (2017).
 - ⁴¹ L. D. Sun, M. Hohage, P. Zeppenfeld, R. E. Balderas-Navarro, and K. Hingerl, *Phys. Rev. Lett.* **96**, 016105 (2006).
 - ⁴² C.-J. Li, Y.-P. Hong, H.-X. Xue, X.-X. Wang, Y. Li, K. Liu, W. Jiang, M. Liu, L. He, R.-F. Dou, et al., *Sci. Rep.* **8**, 404 (2018).
 - ⁴³ D. Go, J.-P. Hanke, P. M. Buhl, F. Freimuth, G. Bihlmayer, H.-W. Lee, Y. Mokrousov, and S. Blügel, *Sci. Rep.* **7**, 46742 (2017).
 - ⁴⁴ P. Torruella, C. Coll, G. Martín, L. López-Coneza, M. Vila, C. Díaz-Guerra, M. Varela, M. L. Ruiz-González, J. Piqueras, F. Peiró, et al., *J. Phys. Chem. C* **121**, 24809 (2017).
 - ⁴⁵ Y. Lu, Y. Huang, Y. Zhang, J.-J. Cao, H. Li, C. Bian, and S. C. Lee, *Appl. Catal. B* **231**, 357 (2018).
 - ⁴⁶ A. Walsh, G. W. Watson, D. J. Payne, R. G. Edgell, J. Guo, P.-A. Glans, T. Learmonth, and K. E. Smith, *Phys. Rev. B* **73**, 235104 (2006).
 - ⁴⁷ M. A. Ordal, L. L. Long, R. J. Bell, S. E. Bell, R. R. Bell, J. R. W. Alexander, and C. A. Ward, *Appl. Opt.* **22**, 1099 (1983).

⁴⁸ L. Debbichi, M. C. Marco de Lucas, J. F. Pierson, and P. Krüger, *J. Phys. Chem. C* **116**, 10232 (2012).

⁴⁹ A. B. Posadas, K. J. Kormondy, W. Guo, P. Ponath, J. Geler-Kremer, T. Hadamek, and A. A. Demkov, *J. Appl.*

Phys. **121**, 105302 (2017).

⁵⁰ D. C. Vaz, P. Noël, A. Johansson, B. Göbel, F. Y. Bruno, G. Singh, S. McKeown-Walker, F. Trier, L. M. Vicente-Arche, A. Sander, et al., *Nat. Mat.* **18**, 1187 (2019).